Fracture behaviour of wood bonded joints under modes I and II by digital image correlation and fibre Bragg grating sensors

J. Xavier[a,b,*], J.R.A. Fernandes[c,d], J.J.L. Morais[a], O. Frazão[d]

[a] *CITAB, Departamento de Engenharias, Escola de Ciências e Tecnologia, Universidade de Trás-os-Montes e Alto Douro, Quinta de Prados, 5001-801 Vila Real, Portugal*

[b] *Optics and Experimental Mechanics Laboratory, INEGI, University of Porto, Campus da FEUP, Rua Dr. Roberto Frias 4200-465 Porto, Portugal*

[c] *Departamento de Física, Escola de Ciências e Tecnologia, Universidade de Trás-os-Montes e Alto Douro, Quinta de Prados, 5001-801 Vila Real, Portugal*

[d] *INESC TEC, Rua do Campo Alegre 687, 4169-007 Porto, Portugal*

Abstract

Direct identification of cohesive laws in modes I and II of wood bonded joints is addressed by the double cantilever beam (DCB) and end-notched flexure (ENF) tests, respectively. Moreover, the development and extension of fracture process zone (FPZ) ahead of the initial crack tip, is analysed by means of digital image correlation (DIC) and embedded fibre Bragg grating (FBG) sensors. From FBG spectral response, the spectrum geometric mean is determined and the strain induced by wavelength variation employed to identify the initial and final stages of the FPZ. These stages are used to consistently define the cohesive laws in both modes I and II. Resistance-curves are determined from the compliance-based beam method (CBBM). Besides, the crack tip opening displacements (CTOD) are determined by post-processing displacement field provided by DIC around the initial crack tip. The strain energy release rate as a function of the CTOD are then determined for both mode I and mode II. The respective cohesive laws are reconstructed by numerical approximation and differentiation. It is concluded that the proposed data reduction scheme is effective to determine both the FPZ development phase and the corresponding cohesive laws of wood bonded joints in both mode I and mode II.

Keywords: wood; adhesion; mechanical testing; joints/joining; digital image correlation; fibre Bragg grating sensors.

1. Introduction

Wood bonded joints have been playing an important role in modern wooden constructions and applications, namely by integrating innovative wood products. However, requirements have been pointed out for enhancing experimental characterisation and modelling of the adhesive bond strength at the adherent wood interfaces. In this framework, the fracture behaviour of wood adhesive joints is of interest, namely by understanding the fundamental constitutive behaviour of the fracture process zone (FPZ) which grows and propagates ahead of crack tip. The complex fracture mechanisms taking place in the FPZ have been handed numerically by means of cohesive zone models (CZM), using interface cohesive finite elements [1]. In this constitutive behaviour, cohesive stresses are related with relative displacements of the adjacent cohesive surfaces [2]. In spite of the utilization of CZM to model several materials, the direct identification of the cohesive laws rises several difficulties. Contrastingly with

---

* Corresponding author.

E-mail address: jmcx@utad.pt (J. Xavier)

inverse method, in which the shape of a particular law is assumed *a priori* and determined by some optimisation by minimizing numerical and experimental global structural response [3-5], direct method do not rely on time consuming modelling updating and are not limited to issues regarding uniqueness of the minimisation solution [8-10]. Besides, the direct approach does not assume *a priori* the shape of the cohesive law. They rely, however, on the measurement of both crack tip opening displacement (CTOD) and the strain energy release rate (*G*) during the fracture test. The cohesive law is then reconstructed by numerical approximation and differentiation of *G* versus CTOD relationship, under the development of the FPZ. This approach was recently applied to wood and composites bonded joints under both mode I [4,11] and mode II [12,13] loading. Resistance-curves (*R*-curves) were determined using the compliance-based beam method (CBBM) [3], whilst the displacement fields ahead of the crack tip were evaluated by means of digital image correlation (DIC) [14-16].

In this work, the direct evaluation of the cohesive laws of *Pinus pinaster* wood bonded joints under modes I and II is analysed. The double cantilever beam (DCB) test was used for mode I loading, whilst the end-notched flexure (ENF) test was selected for mode II loading. The proposed identification method is based on measurements provided by both digital image correlation (DIC) and fibre Bragg grating (FBG) sensors. The analysis of the FBG, embedded in the glue line, was employed to define the initial and final stages of the formation and development of the fracture process zone (FPZ). A data reduction scheme based on the compliance-based beam method (CBBM) was used for both DCB and ENF fracture tests. In this method only the load-displacement curve needs to be measured for the evaluation of the resistance-curve (*R*-curve), since it is based on an equivalent elastic crack length (a_e). The CTOD was determined by post-processing the displacement fields around the crack tip. By combining these measurements, the cohesive laws in both mode I and mode II of wood bonded joints was directly evaluated.

1. Data reduction

2.1 DCB test

The strain energy release rate under mode I (G_I) is determined from the tensile stress (σ_I) and CTOD (w_I) according to the following relationship [17]

$$G_I = \int_0^{w_I} \sigma_I(\overline{w}_I)\, d\overline{w}_I . \qquad (1)$$

Accordingly, the cohesive law in mode I can be determined by

$$\sigma_I(w_I) = \frac{\partial G_I}{\partial w_I} \qquad (2)$$

To solve Eq. (2) both G_I and w_I must be determined during a mode I opening fracture test. The DCB test was selected as schematically shown in Fig. 1a. The DCB specimen consists of two rectangular beams glued together by an adhesive. To analyse fracture in mode I, a horizontal crack surface of length a_0 is initially introduced. The strain energy release rate (G_I) can be determined by the Irwin-Kies equation as [18]

$$G_I = \frac{P^2}{2B}\frac{dC}{da} \qquad (3)$$

where *P* is the global applied load, *B* is the width of the specimen, *C* is the compliance and *a* stands for crack length during test. The CBBM is a data reduction scheme that allows the calculation of d*C*/d*a*, avoiding the actual measurement of *a* during the test [3]. In this method, *C* is given explicitly as a function of *a* by the following relationship [3]

$$C = \frac{8a^3}{Bh^3 E_L} + \frac{12a}{5BhG_{LR}} \qquad (4)$$

where E_L and G_{LR} represent the elastic longitudinal and shear moduli, respectively, which can be determined independently from either homogeneous [19,20] or heterogeneous [21,22] tests.

In order to cope with the natural material variability, the presence of adhesive, and the stress concentration in the vicinity of the crack tip, Eq. (4) can be firstly solved to an equivalent elastic modulus (E_f) by using

the initial crack length (a_0) and specimen compliance (C_0) in Eq. (4)

$$E_f = \frac{8(a_0 + h\Delta)^3}{Bh^3}\left(C_0 - \frac{12(a_0 + h\Delta)}{5BhG_{LR}}\right)^{-1} \quad (5)$$

where Δ is a crack length correction that accounts for root rotation elastic effects. This parameter can be obtained numerically [23].

During the crack formation and propagation, Eq. (4) is employed to determine an equivalent elastic crack length (a_e) from the current specimen compliance (C). The R-curve in mode I is therefore obtained by combining Eqs. (3-5)

$$G_I = \frac{6P^2}{B^2 h}\left(\frac{2a_e^2}{E_f h^2} + \frac{1}{5G_{LR}}\right) \quad (6)$$

In order to apply Eq. (2) the measurement of the CTOD is mandatory. A solution is provided by post-processing DIC displacements according to the following relationship [16,24]

$$w_I = \left\| w_I^+ - w_I^- \right\| \quad (7)$$

where w_I^+ and w_I^- are the components of the displacement in the direction perpendicular to the crack propagation, associated to the upper and the lower cracked surface. In practice, a subset is first selected at the initial crack tip, and a pair of points nearby are used for measuring the CTOD during the fracture test.
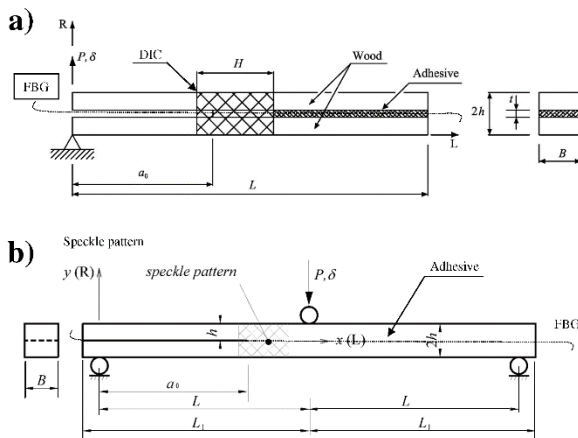
a)

b)

Fig. 1. Schematic representation of the (a) DCB test; (b) ENF test.

2.2 ENF test

The strain energy release rate under mode II (G_{II}) is obtained from the shear stresses (σ_{II}) and CTOD (w_{II}) as

$$G_{II} = \int_0^{w_{II}} \sigma_{II}(\overline{w}_{II})\,d\overline{w}_{II} \quad (8)$$

Inversely, the cohesive law in mode II is determined by differentiation of Eq. (8) yielding

$$\sigma_{II}(w_{II}) = \frac{\partial G_{II}}{\partial w_{II}} \quad (9)$$

In practice, the solution of Eq. (9) requires the evolution of G_{II} with regard to w_{II} during a mode II fracture tests. The ENF test was proposed in this work, as schematically shown in Fig. 1b. A pre-cracked surface of initial crack length (a_0) of $0.7L$ [25] is assumed in the specimen to allow self-similar crack propagation during a certain extent.

Classical data reduction schemes typically require the measuring of the crack length (a) during the fracture test together with load and displacement. In order to overcome these drawbacks, the CBBM was used. Assuming beam theory with shear effects, the specimen compliance during crack propagation can be written as [26]

$$C = \frac{3a_{eq}^3 + 2L^3}{12E_f I} + \frac{3L}{5G_{LR}A} \quad (10)$$

with

$$a_{eq} = a + \Delta a_{FPZ} \quad (11)$$

where Δa_{FPZ} is the crack length correction accounting for the FPZ effect, G_{LR} is the shear modulus and $A = 2hB$ and $I = 8Bh^3/12$ are, respectively, the cross-section area and the second moment of area (Fig. 1b). It is noticed, that Eq. (10) can be used for estimating the flexural modulus (E_f) of each specimen, considering the initial crack length (a_0) and initial compliance (C_0). Therefore, during crack propagation the equivalent crack length can be obtained from

$$a_{eq} = a + \Delta a_{FPZ} = \left[\frac{C_{corr}}{C_{0_{corr}}}a_0^3 + \frac{2}{3}\left(\frac{C_{corr}}{C_{0_{corr}}} - 1\right)L^3\right]^{\frac{1}{3}} \quad (12)$$

with

$$C_{\text{corr}} = C - \frac{3L}{5G_{\text{LR}}A} \qquad C_{0_{\text{corr}}} = C_0 - \frac{3L}{5G_{\text{LR}}A}. \qquad (13)$$

Considering the Irwin-Kies Eq. (3). The strain energy release rate G_{II} can then be obtained as

$$G_{\text{II}} = \frac{9P^2}{16B^2 E_f h^3} \left[\frac{C_{\text{corr}}}{C_{0_{\text{corr}}}} a_0^3 + \frac{2}{3} \left(\frac{C_{\text{corr}}}{C_{0_{\text{corr}}}} - 1 \right) L^3 \right]^{2/3} \qquad (14)$$

The w_{II} parameter must be measured experimentally by a suitable method. In this work, w_{II} was determined by post-processing DIC measurements according to the following relationship [13]

$$w_{\text{II}} = \left\| w_{\text{II}}^+ - w_{\text{II}}^- \right\| \qquad (15)$$

here w_{II}^+ and w_{II}^- are the components of the displacement in the direction of the crack propagation associated to the upper and the lower cracked surface.

2. Experimental work

3.1 Material and testing

The wood material used in this work was taken from a single *Pinus pinaster* tree. Logs were conditioned to a moisture content of about 12%. Matched beams were then cut from mature wood to mitigate material variability.

DCB wood-bonded joints specimens were then prepared with nominal dimensions of $2h = 20$ mm, $B= 20$ mm, $t = 0.1$ mm, $L = 500$ mm and an initial crack length of $a_0 = 100$ mm (Fig. 1a). ENF wood-bonded joints specimen test were prepared with $2L = 460$ mm, $a_0 = 162$ mm, $h = 15$ mm, $B = 20$ mm, $t = 0.2$ mm. The wood surfaces were firstly cleaned and polished using sandpaper to enhance adhesion with the epoxy adhesive (Araldite® 2015). The pre-crack surface within the adhesive was introduced by means of a thin Teflon® film (thickness of 25 μm).

The fracture tests were carried out in a screw-driven Instron® 1125 testing machine at crosshead displacement rate of 5 mm/min. The applied load was measured by means of a 100 kN load cell. The load (P) and the crosshead displacement of the testing machine (δ) were recorded during the test by means of a National Instruments® USB-6210 daq card controlled using Labview®, with a sampling rate of 10

Hz, connected to the analogue outputs of the testing machine. The fracture tests were coupled with DIC in order to determine the displacement fields at the crack tip as described in the following.

3.2 Digital image correlation

DIC is a full-field measurement technique in which displacements of a target speckled pattern are determined by correlating images at different mechanical configurations [27]. A speckle pattern was painted over a region of interest, around and ahead of the initial crack tip, by means of an airbrush to achieve suitable grain size, contrast and isotropy at the scale of observation. The ARAMIS® DIC-2D system was used in this work [28,29]. The optical system components and DIC measuring parameters are summarised in Table 1. A charged coupled digital (CCD) camera coupled with a telecentric lens was used for image grabbing. According to the typical size of the painted speckle pattern, a subset size of 15×15 pixels² was chosen yielding a spatial resolution of 0.27×0.27 mm². The accuracy in displacement of the order of 1-2×10⁻² pixel (0.18-0.36 μ m) was achieved [29,30]. A pair of points were selected for CTOD evaluation at the initial crack tip, with an initial vertical distance of about 0.5 mm.

3.3 Fibre Bragg grating sensors

Fibre Bragg grating sensors (FBGs) have been used as a strain sensor in many engineering applications. One intrinsic advantage is related to the sensor dimension due to the fibre diameter (125 μm for a standard SMF28 fibre). For the purpose of this study, FBGs with a length of 6 mm were produced by the phase mask technique using a KrF excimer laser emitting 24 ns pulses with wavelength of 248 nm.

Table 1. Components of the optical system and digital image correlation measuring parameters

CCD camera	
Model	8 bits Baumer Optronic FWX20 (1624×1236 pixels²)
Acquisition frequency	1 Hz
Lens	
Model	Opto Engineering Telecentric lens TC 23 36
Field Of View (1/1.8")	29.3×22.1 mm²
Working Distance	103.5±3 mm
Conversion factor	0.018 mm/pixel
Lighting	Raylux 25 white-light LED
DIC measurements	
Subset size	15×15 pixel² (0.270×0.270 mm²)
Subset step	13×13 pixel² (0.234×0.234 mm²)
Resolution	1-2 ×10⁻² pixel (0.18-0.36 μm)

These sensors were manufactured by Fibersensing®, with the Bragg peak at 1550 nm and a peak reflectivity higher than 90%. The fibre with FBG was embedded in the glue line, during the specimen manufacture, ensuring that the sensor was positioned at the centre of initial crack tip and oriented along the longitudinal direction of specimen (Fig. 1). The correct alignment of optical fibre was assured using dead weights attached to its extremities, while pressing the two arms of DCB specimen during the adhesive cure. The fibre was connected to a spectral analyser Fibersensing® Bragmeter FS2200SA that retrieved reflection spectra with a frequency of 0.5 Hz. This system makes the FBG interrogation in the 1500-1600 nm range and can record simultaneously the reflection and transmission spectra. The spectral analyzer and the daq card were controlled by the same computer and all the data acquired by these two systems were temporally synchronised.

3. Results and discussion

Fig. 2 shows typical load-displacement curves for both DCB and ENF tests. As it can be observed, both curves have a linear behaviour followed by a non-linear path until maximum load is reached. The non-linear behaviour is induced by the formation of a FPZ ahead of the initial crack tip [31]. Crack propagation is assumed to occur during the monotonically loading decrease.

Fig. 3 represents the CTOD as a function of the applied displacement (δ) for both DCD and ENF tests. Typically, the CTOD-δ curve show three distinct regions, defined by a clear change in its slope, in accordance with the macroscopic behaviour of the P-δ curve. In a first stage, the CTOD increases at a constant rate, corresponding to the initial elastic response. A second region is defined by an increased rate which is associated to the development of FPZ. In the last region the curve changes again of slope, typically associated with steady-state crack propagation.

The nature and sequence of damage events described above, inferred from the experimental P-δ and CTOD-δ curves, was also examined using the reflected spectral response of the FBG sensor embedded in the glue line at the initial crack tip. The reflection spectra are difficult to interpret due to peak splitting and the appearance of multiple reflection peaks of equivalent height [32]. Several methods have been proposed to reconstruct the multi-axial strain field applied to the FBG. However, these techniques are, in general, very time consuming and provide limited information of the specimen overall mechanical behaviour [33]. To determine the spectral shift the standard methods try to identify one maximum reflection peak per FBG and follow the position of this peak in time [34]. However, if the reflected spectrum is becoming highly deformed with multiple peaks splitting, each FBG will yield multiple peaks with equivalent heights resulting in inconsistent values for the spectrum wavelength shift evolution. It was also observed that the overall FBG spectral reflection response always moves toward higher wavelengths with the increase of applied deformation, even if it was not possible to identify a predominant reflection peak that can be followed and used to quantify this overall wavelength shift. This problem was tackled by the use of an alternative method to quantify the FBG spectral wavelength shift using the spectral wavelength geometric mean (λ_{GM}) that can be determined for all the measured spectra. The evolution of this wavelength geometric mean can be followed in time and then related with the other macroscopic quantities measured simultaneously during the DCB test.

In this method, each spectrum is divided in m optical power levels, between 10% and 95% of maximum FBG reflected power (p_{max}). The geometric mean of each power level (p_i) is determined by

$$\lambda_j^{avg} = \sqrt[n]{\prod_{i=1}^{n} \lambda_i} \ . \tag{16}$$

using the n wavelengths (λ_i) that satisfy the inequality $p \geq pi$. The number of terms satisfying this condition will vary among power levels and, as a consequence, the root order will also vary accordingly. The final wavelength representing each spectrum is then determined by calculating the geometric mean of the wavelengths representing the m power levels by

$$\lambda_{GM} = \sqrt[m]{\prod_{i=1}^{m} \lambda_j^{avg}} \ . \tag{17}$$

By using this method the power distribution is taken into account because wavelengths with higher power levels will contribute more to the final mean value than wavelengths with lower power levels. The mean wavelength shift ($\Delta\lambda_{GM}$) is related to the mean local strain at the crack tip (ε) by the following equation [35]

$$\varepsilon = \frac{1}{1 - p_e} \frac{\Delta\lambda_{GM}}{\lambda_{GM0}} \tag{18}$$

where $p_e = 0.22$ is the photo-elastic coefficient for standard Ge-doped optical fibres and λ_{GM0} is the initial (before the fracture test) value of λ_{GM}.

The variation of the mean local strain (ε) with regard to the applied displacement (δ) is shown in Figs. 2 and 3, together with the P-δ curve and the CTOD-δ curve, respectively. A noticeable rise in the local strain rate is observed, in close agreement with the increase of CTOD growth rate (Fig. 3), after the end of the initial elastic segment of P-δ curve (Fig. 2). That change of local strain rate is understood as an indicator of the onset of FPZ development. Hence, the following criterion for the initiation of FPZ can be stated from the ε -δ curve: it is the displacement δ_i obtained from the intersection of two straight lines adjusted to the ε -δ data points, before and after the main slope augmentation of ε -δ curve. This criterion is translated to a point (square point) in the P-δ curve (Fig. 2) and in the CTOD-δ curve (Fig. 3), showing its consistency.
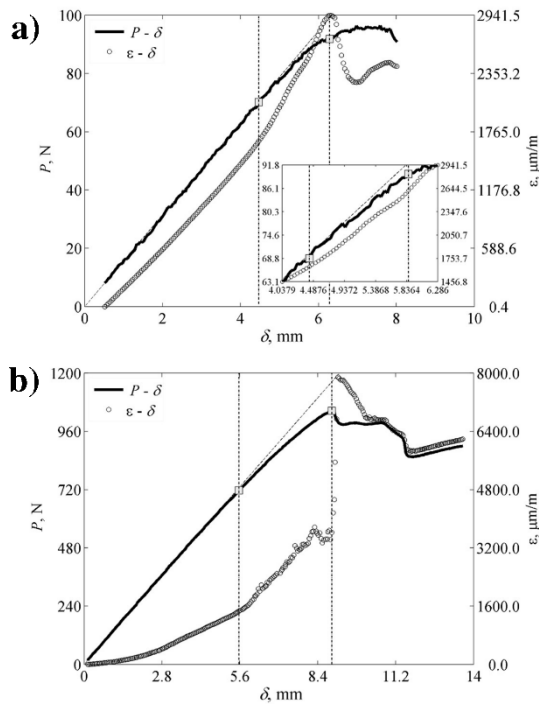

Fig. 2. Load and mean strain curves as a function of the applied displacement: (a) mode I (DCB test); (b) mode II (ENF test).

As it can be seen in Fig. 3, in the neighbourhood of the maximum load applied to the specimen (for this specimen, the square point slightly after the maximum load) the ε -δ curve attains a maximum value, which is followed by a negative slope. This negative slope represents a strain relaxation which could be attributed to the start of crack advance and to the end of FPZ growth.
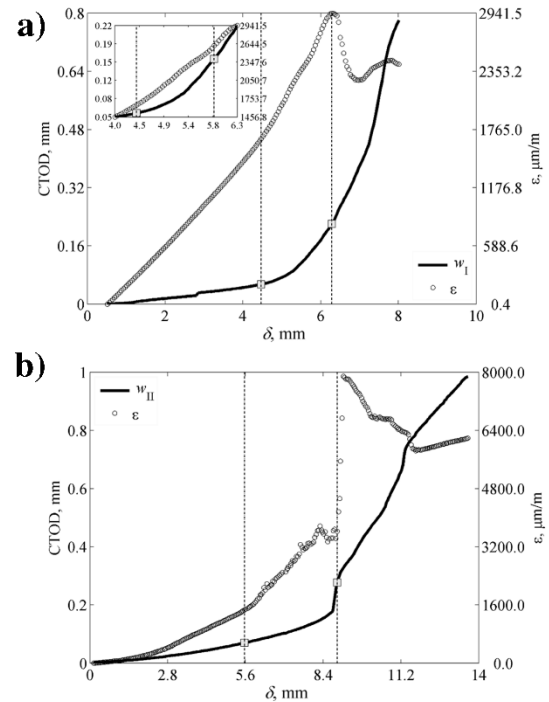

Fig. 3. Crack tip opening displacement and mean strain curves as a function of the applied displacement: (a) mode I (DCB test); (b) mode II (ENF test).

The displacement δ_e matching the maximum ε value (or the first sign change of ε -δ slope) can be employed as a criterion to define the full development of FPZ. The CTOD value associated to δ_e is represented by a square point in Fig. 4. As it can be seen, this point is the boundary between the second and third regions of CTOD-δ curve discussed above.

The wavelength peak (or Bragg wavelength) is a very sensitive parameter and its value can be measured accurately when the applied strain is uniform along the grating. However, during the fracture test the spectral response becomes very complex due to the presence of non-uniform axial strains, displaying split-peak or multiple-peaks, with no simple means of interpretation. Moreover, the shape of FBG reflection spectrum changes considerably during the fracture test, according to the local damage events. Despite the complex form and evolution of FBG reflection spectrum throughout the fracture test, the geometric mean wavelength λ_{GM} (or the related local mean strain, obtained through Eq. 18) proves to be an effective way to determine the limits, in terms of the independent testing variable (i.e. the applied displacement), of FPZ development [36].
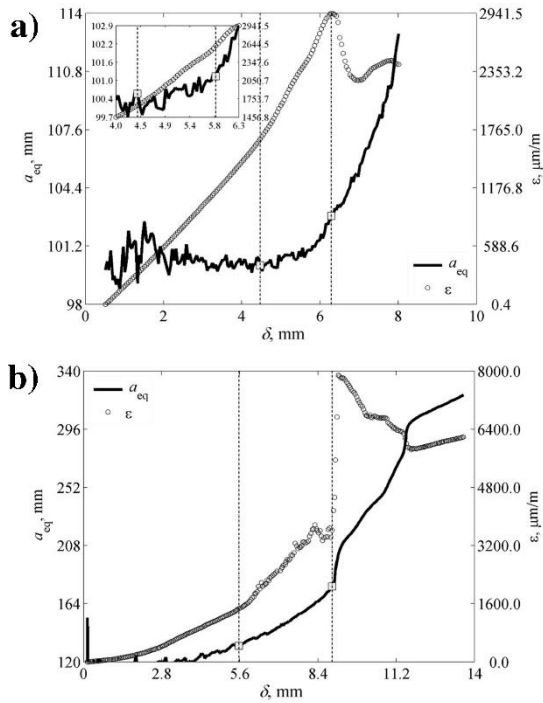
Fig. 4. Equivalent crack length and mean strain curves as a function of the applied displacement: (a) mode I (DCB test); (b) mode II (ENF test).

It is important to note that the FBG sensor length does not influence the detection of the onset of FPZ growth. In both fracture tests (DCB and ENF tests) the change in slope of ε-δ curve is a reliable indicator of this event. However the FBG sensor length influences the behaviour of the ε-δ curve in the neighbourhood of maximum load applied, as can be concluded from the results of Figure 4. For DCB specimens the length of FPZ (about 3mm, as estimated from the change in a_e between the square marks on Figure 4a) is lesser than the length of FBG sensor (6mm) and a smooth transition of ε-δ curve was registered around the maximum value of ε. For the ENF specimens the estimated length of FPZ (about 40mm, Figure 4b) is greater than the FBG sensor length and a sharp change of the mean local strain (ε) at the start of crack advance was registered (Figure 4b). Notwithstanding the relation between the FBG sensor size and the FPZ size, the maximum ε value (or the first sign change of ε-δ slope) is a consistent criterion to define the end of FPZ development phase. Therefore, the identification of mode I and mode II cohesive laws can be performed using the P, δ and CTOD experimental values within the limits identified from the geometric mean value of the wavelength shift of FBG reflected spectral response.
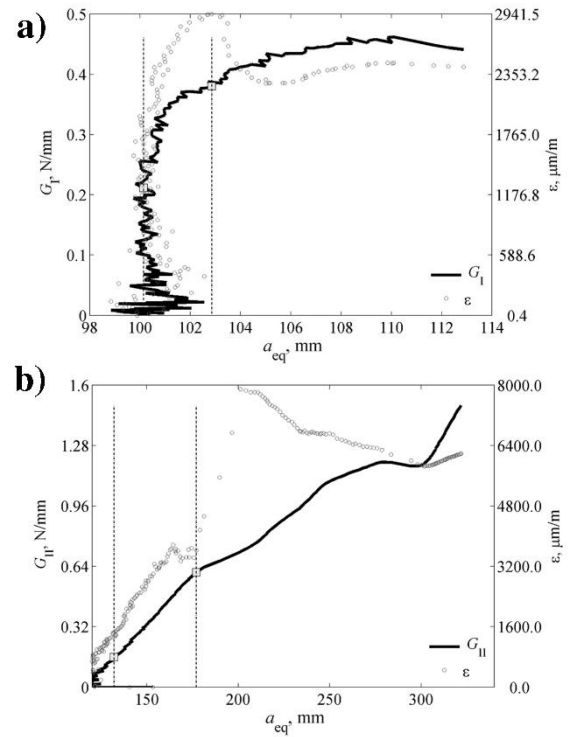

Fig. 5. Resistance and mean strain curves as a function of the equivalent crack length: (a) mode I (DCB test); (b) mode II (ENF test).

The first step in applying the CBBM is the evaluation of the equivalent elastic crack length (a_e) from the P-δ curve. Fig. 4 shows the variation of a_e with the applied displacement, together with the ε -δ curve, for both DCB and ENF tests. The first significant value of a_e occurs at the onset of FPZ and is equal to the initial crack length (a_0). In the early stages of linear elastic response of specimens the calculated values of a_e are noisily and its evolution with the applied displacement is meaningless. After the onset of FPZ, a_e advances at a growing rate, until a constant propagation rate is achieved. It is remarkably noted that the transient region of equivalent crack propagation (i.e., the region where da_e/dt is growing) matches with the FPZ growth identified in the ε -δ curve. This behaviour was systematically observed among the tested specimens. The second step of the data reduction is the evaluation of the R-curve. The obtained results can be seen in Fig. 5, where the λ_{GM} versus a_e relationship is also superimposed. An initial (G_{Ii}) and critical (G_{Ic}) strain energy release rates in mode I were evaluated from the R–curves afterwards. G_{Ii} is assumed to be the value of strain energy release rate at δ_i whereas G_{Ic} is assumed to be the strain energy release rate at δ_e, just before steady-state crack

propagation. It is worth noticing that the ε-a_e curve exhibits the same trend of the *R*-curve, in the pre-FPZ development region and in the post-FPZ development region.

Fig. 6(left) shows the evolution of the strain energy release rate with regard to the CTOD on both mode I and mode II, obtained by combining CBBM and DIC measurements. This type of curve is the basic information required for the direct identification of the cohesive laws (Fig. 6(right)). A continuous function (the logistic function) was used to approximate the

data points in the reconstructing process of the cohesive law [36], as shown in Fig. 6. This procedure allows filtering the experimental data before analytical differentiation, thus circumventing the noise amplification characteristic of numerical differentiation. Only the data points within the limits of FPZ development were taken into account in the regression analysis. The cohesive laws were then determined by analytical differentiation of the logistic approximation function, as shown in Fig. 6.
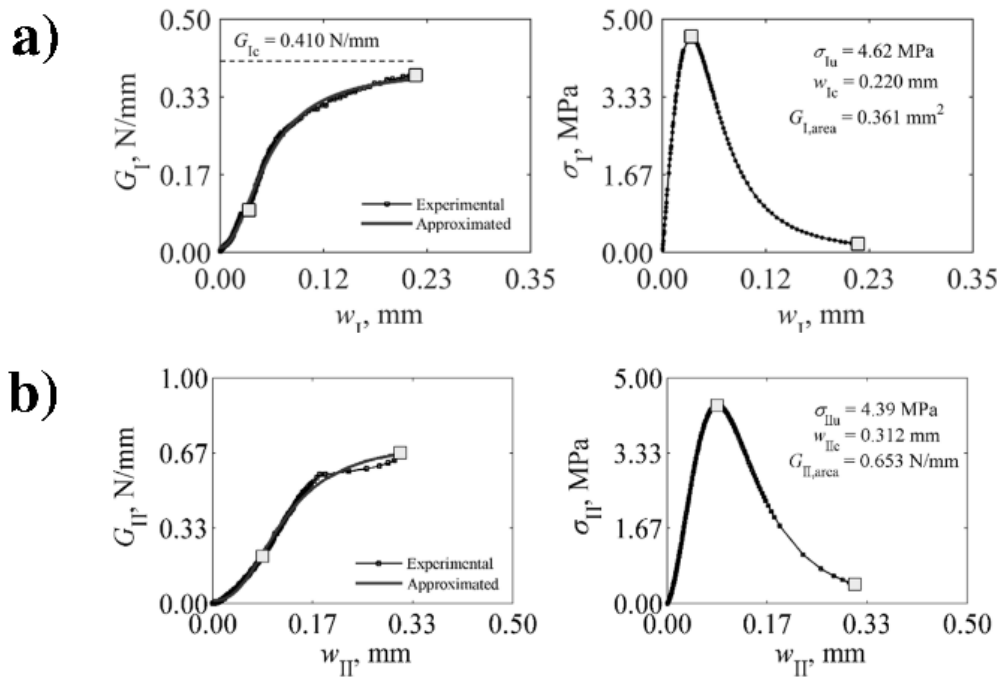

Fig. 6. Strain energy release rate as a function of CTOD and cohesive law identification: (a) mode I (DCB test); (b) mode II (ENF test).

4. Conclusions

In this work the direct characterisation of the cohesive law in both mode I and mode II of *P. pinaster* wood bonded joints is addressed. The DCB and ENF fracture tests were selected for mode I and mode II loading, respectively. Both type of specimens were instrumented using digital image correlation (DIC) and fibre Bragg grating (FBG) sensors embedded in the glue line. The CBBM was consistently used for determining the strain energy release rate in mode I (G_I) and mode II (G_{II}) from the global response of the material measured in terms of the *P-δ* curves. DIC measurement allowed the determination of the crack

tip opening displacement in mode I (w_I) and mode II (w_{II}) with suitable balance between spatial resolution and resolution. The cohesive laws in mode I (σ_I-w_I) and mode II (σ_{II}-w_{II}) were determined following a numerical reconstruction and differentiation algorithm based on the G_I-w_I and G_{II}-w_{II} relationships, respectively. The geometric mean value of the wavelength shift of FBG reflected spectral response was used to detect the development of fracture process zone (FPZ). The actual extension of this region is very difficult to assess experimentally. However, a post-processing analysis of the FBG reflected spectral response allowed a consistent length extension evaluation of the formation of the FPZ.

Acknowledgements

References

[1] M. Elices, G.V. Guinea, J. Gomez, J. Planas, *Eng. Fract. Mech.* **69**, 137 (2002).

[2] A. Needleman, ASME *J Appl. Mech.* **54** (1987).

[3] M.F.S.F. de Moura, J.L. Morais, N. Dourado, *Eng. Fract. Mech.* **75,** 978 (2008).

[4] F.G.A. Silva, J. Xavier, F.A.M. Pereira, J.J.L. Morais, N. Dourado, M.F.S.F. de Moura, *Holzforschung* **67**, 913 (2013).

[5] R.D.S.G. Campilho, M.D. Banea, J.A.B.P. Neto, L.F.M. da Silva, *J. Adhesion* **88**, 513 (2012).

[8] L. Andena, M. Rink, J.G. Williams, *Eng. Fract. Mech.* **73**, 2476 (2006).

[9] V. Slowik, B. Villmann, N. Bretschneider, T. Villmann, *Comput. Method Appl. Me.* **195**, 7223 (2006).

[10] B.F. Sørensen, E.K. Jacobsen, *Compos. Part A-Appl. S.* **29**, 1443 (1998).

[11] G.F. Dias, M.F.S.F. de Moura, J.A.G. Chousal, J. Xavier, *Compos. Struct.* **106**, 646 (2013).

[12] F. Silva, J. Morais, N. Dourado, J. Xavier, F.A.M. Pereira, M.F.S.F. de Moura, *Int. J. Adhes. Adhes.* **51**, 54 (2014).

[13] R.M.R.P. Fernandes, J.A.G. Chousal, M.F.S.F. de Moura, J. Xavier, *Compos. Part B-Eng.* 52, 269 (2013).

[14] A.M.R. Sousa, J. Xavier, J.J.L. Morais, V.M.J. Filipe, M.Vaz, *Opt. Laser Eng.* **49**, 1402 (2011).

[15] J. Xavier, A.M.R. Sousa, J.J.L. Morais, V.M.J. Filipe, M. Vaz, *Opt. Eng.* **51**, 043602 (2012).

[16] J. Xavier, J. Oliveira, P. Monteiro, J.J.L. Morais, M.F.S.F. de Moura, *Exp. Mech.* **54**, 829 (2014).

[17] S.P. Fernberg, L.A. Berglund, *Compos Sci. Technol.* **61**, 2445 (2001).

[18] G.R. Irwin, J.A. Kies, *Weld Res. Suppl.* **33**, 193 (1952).

[19] J.C. Xavier, N.M. Garrido, M. Oliveira, J.L. Morais, P.P. Camanho, F. Pierron, *Compos Part A-Appl. S.* **35**, 827 (2004).

[20] J. Xavier, M. Oliveira, J. Morais, J. Pinto, *Holzforschung* **63**, 217 (2009).

[21] J. Xavier, S. Avril, F. Pierron, J. Morais, *Holzforschung* **61**, 573 (2007).

[22] J. Xavier, S. Avril, F. Pierron, J. Morais, *Compos Part A-Appl. S.* **40**, 1953 (2009).

[23] J. Xavier, P. Monteiro, J. Morais, N. Dourado, M.F.S.F. de Moura, *J. Mater. Sci.* **49**, 7371 (2014).

[24] G. Catalanotti, P.P. Camanho, J. Xavier, G. Dávila A.T. Marques, *Compos. Sci. Technol.* **70**, 1986 (2010).

[25] L.A. Carlsson, J.W. Gillespie, R.B. Pipes, *J. Compos. Mater.* **20**, 594 (1986).

[26] M.F.S.F. de Moura, M.A.L. Silva, J.J.L. Morais, A.B. de Morais, J.J.L. Lousada, *Holzforschung* **63**, 99 (2009).

[27] B. Pan, K. Qian, H. Xie, A. Asundi. *Meas. Sci. Technol.* **20**, 062001 (2009).

[28] ARAMIS, User Manual - Software - v6.0.2-6, 2009.

[29] J. Xavier, A.M.P. de Jesus, J.J.L. Morais, J.M.T. Pinto, *Constr. Build. Mater.* **26**, 207 (2012).

[30] A.M.R. Sousa, J. Xavier, M. Vaz, J.J.L. Morais, V.M.J. Filipe, *Strain* **47**, 87 (2011).

[31] N. Dourado, S. Morel, M.F.S.F. de Moura, G. Valentin, J. Morais, *Compos. Part A-Appl. S.* **39**, 415 (2008).

[32] S. Stutz, J. Cugnoni, J. Botsis, *Eng. Fract. Mech.* **78**, 890 (2011).

[33] R.S. Maciel, O. Frazão, J.J.L. Morais, J.R.A. Fernandes. Proc. SPIE 8785, 8th Ibero American Optics Meeting/11th Latin American Meeting on Optics, Lasers, and Applications, 8785FQ, 2013.

[34] J. Jiang, T. Liu, K. Liu, Y. Zhang, *Opt. Eng.* **51**, 034403 (2012).

[35] J. Botsis, L. Humbert, F. Colpo, P. Giaccari, *Optics Laser Eng.* **43,** 491 (2005).

[36] J. Xavier, J.R.A. Fernandes, O. Frazão, J.J.L. Morais, *Compos. Struct.* **121**, 83 (2015).